# Transformation of energy spectrum and wave functions on the way from a 2D-to-3D topological insulator in HgTe quantum wells

G. M. Minkov,[1,2] V. Ya. Aleshkin,[3,4] O. E. Rut,[1] A. A. Sherstobitov,[1,2] S. A. Dvoretski,[5]
N. N. Mikhailov,[5,6] and A. V. Germanenko [1]

[1]*School of Natural Sciences and Mathematics, Ural Federal University, 620002 Ekaterinburg, Russia*
[2]*M. N. Mikheev Institute of Metal Physics of Ural Branch of Russian Academy of Sciences, 620137 Ekaterinburg, Russia*
[3]*Institute for Physics of Microstructures RAS, 603087 Nizhny Novgorod, Russia*
[4]*Lobachevsky University of Nizhny Novgorod, 603950 Nizhny Novgorod, Russia*
[5]*Institute of Semiconductor Physics RAS, 630090 Novosibirsk, Russia*
[6]*Novosibirsk State University, Novosibirsk 630090, Russia*

A magnetotransport and quantum capacitance of the two-dimensional (2D) electron gas in HgTe/Cd$_x$Hg$_{1-x}$Te quantum wells of a width (20.2–46.0) nm are experimentally investigated. It is shown that the first energy subband of spatial quantization is split due to the spin-orbit interaction and the split branches are single spin, therewith the splitting strength increases with the increase of the quantum well width. The electron effective masses in the branches are close to each other within the actual density range. Magnetointersubband oscillations (MISO) observed in the structures under study exhibit the growing amplitude with the increasing electron density that contradicts to the expected decrease of wave-function overlap for the rectangular quantum well. To interpret the data obtained, we have used a self-consistent approach to calculate the electron energy spectrum and the wave function within framework of the $kP$ model. It has been, in particular, shown that the MISO amplitude increase results from the increasing overlap of the wave functions due to their shift from the gate electrode with the gate voltage increase known as a phenomenon of the negative electron polarizability. The results obtained from the transport experiments are supported by quantum capacitance measurements.

## I. INTRODUCTION

Structures with HgTe quantum wells (QWs) are attracting a lot of attention for many reasons. First, the QW is a gapless semiconductor, while the barriers Hg$_{1-x}$Cd$_x$Te are a semiconductor with a normal band ordering [1,2]. Second, the band spectra of the parent materials HgTe and Hg$_{1-x}$Cd$_x$Te have been studied in detail and their parameters are fairly well known. Third, as shown in numerous papers (see, e.g., [3–8] and references therein) different types of spectrum are realized depending on the QW width ($d$). At $d = d_c \simeq 6.3$ nm it is gapless [3] and close to the linear Dirac-type spectrum at small quasimomentum [6]. When QW is narrow, $d < d_c$, the ordering of energy subbands of spatial quantization is analogous to that in conventional semiconductors; the highest valence subband at $k = 0$ is formed from the heavy-hole $\Gamma_8$ states, while the lowest conduction subband is formed both from the $\Gamma_6$ states and light-hole $\Gamma_8$ states. For a thicker HgTe layer, $d > d_c$, the quantum well is in the inverted regime; the lowest conduction subband is formed from the heavy-hole $\Gamma_8$ states [9], whereas the subband formed from the $\Gamma_6$ states and light-hole $\Gamma_8$ states sinks into the valence band. In the inverted regime, the spectrum becomes semimetallic at $d \gtrsim 15$ nm due to overlapping of the valence and conduction bands, therewith the semimetallic phase is a universal property independent of the surface orientation, but is very sensitive to the strain effects

caused by the lattice mismatch of HgTe and Hg$_{1-x}$Cd$_x$Te [10–12]. Fourth, the theory predicts that at $d > 6.5$ nm, the QW will be a two-dimensional (2D) topological insulator when, along with two-dimensional states, one-dimensional edge states are formed. Fifth, the HgTe/Hg$_{1-x}$Cd$_x$Te system is a good candidate for realizing of a three-dimensional (3D) topological insulator. As known the inversion of the $\Gamma_6$ and $\Gamma_8$ band ordering in HgTe is the origin of existence the 2D states on the surface of the bulk material [9]. But since the mercury telluride is semimetal, these states are always coupled to metallic bulk states. However, with applied uniaxial strain, a gap opens up between the light-hole and heavy-hole bands, so that strained 3D HgTe is a true 3D topological insulator [13]. In the HgTe/Hg$_{1-x}$Cd$_x$Te structure, uniaxial strain is of natural origin due to lattice mismatch HgTe and Hg$_{1-x}$Cd$_x$Te. The critical thickness for lattice relaxation is around 200 nm [14], implying that for thinner HgTe the epilayer adopts the lateral lattice constant of the substrate, while in thicker layers the strain is relaxed by the formation of dislocations. It is generally accepted that the HgTe QW behaves like 3D top insulator already at $d \simeq (70$–$80)$ nm [14,15] that allows ones to trace the transformation of the physical properties of HgTe/Hg$_{1-x}$Cd$_x$Te system on the way from 2D-to-3D topological insulator with thickening of the HgTe layer.

In addition, the technology of growing HgTe/Hg$_{1-x}$Cd$_x$Te structures is well developed [16–18] which makes it possible

to grow structures with high-mobility electrons and holes. Multiband *kP* calculations of the spectrum and wave functions are well developed and tested. This would seem to make it possible to understand all the properties (transport, optical, etc.) of such structures.

Experimentally, the energy spectrum of structures with $d = (4–20)$ nm has been studied in sufficient detail by various techniques including the optical and photoelectric methods in a wide range of radiation wavelength, starting from the terahertz range [19–22], magnetotransport [15,23–26]. It was shown that in general the energy spectrum is reasonably described within the framework of the *kP* model, in which the spin-orbit (SO) interaction is taken into account. The main contribution to SO interaction comes from the asymmetry of the interfaces for the valence band [27,28] and from the Bychkov-Rashba effect for the conduction band [4,29]. But, some discrepancies remain; the experimental effective mass of electrons at the bottom of the conduction band at $d = (10–20)$ nm turns out to be 1.5–2 times less than the theoretical one (the authors of Ref. [2] assume that this is due to many-particle effects).

Many papers have been devoted to the study of conductivity by the edge states [30–33], which should be topologically protected from backscattering according to theoretical predictions [34–37]. However, in most experiments, the mean-free path for such states did not exceed (1–3) $\mu$m, which is not much greater than the mean-free path of two-dimensional electrons ($L_p$) in these structures [$L_p = (0.5–5)$ $\mu$m for $\mu = (10^5–10^6)$ cm$^2$/Vs, $n = 1 \times 10^{11}$ cm$^{-2}$]. Another prediction of the theory concerns the specific features of the spectrum and wave functions in wide HgTe quantum wells. It was predicted [38] that single-spin surface states should exist in sufficiently wide quantum wells, which are well localized at the boundaries of the quantum well. Studies of such structures have attracted a lot of attention of experimenters [15,39–41]. Structures with a QW width of (60–90) nm were mainly studied. Only the phenomenological model of surface states was used to interpret the data. No quantitative comparison with theoretical calculations was made.

Let us consider what are specific features of the methods used to study the spectrum, its transformation with increasing width, and the properties of states caused by a nontrivial topology.

In interband optics and magneto-optics experiments, both the valence band and the conduction band participate in the processes. But, the valence band has a complex spectrum, which makes it difficult to interpret experimental data.

When studying the low-temperature transport, the spectrum at the Fermi level is probed. The Fermi energy can be easily changed, if you are investigating gated structures by changing the gate voltage ($V_g$). But, in this case, the gate voltage changes not only the carrier density, and hence the Fermi energy, but also the potential profile of QW. To interpret the results in this case, it is necessary to solve the self-consistent problem taking into account the real potential, which changes significantly with a change of the gate voltage.

In principle, the Fermi energy can be changed by doping, but even in this case, it is imperative to take into account the electrostatic potential of the charge carriers and the doping impurities, i.e., to solve a self-consistent problem when

interpreting the data quantitatively. In addition, these will be different samples, the asymmetry of which is difficult to determine and change.

In almost all the experimental studies of the magnetotransport in wide QWs ($d > 15–20$ nm), structures with the gate were studied, and the results were analyzed using an intuitive model in which it is assumed that near each of the walls there are single-spin states at some distance from the wall of some width $L_z$, which are independent of $V_g$ and shift only in the energy by applied gate voltage [26,42,43]. The accuracy of this approach, especially for sufficiently wide QWs, remains unclear.

To understand how the energy spectrum and wave functions of states change with an increase in the QW width, in this work we have experimentally studied the magnetotransport phenomena and the dependence of the capacitance between 2D gas and the gate electrode in a wide range of gate voltages in practically unexplored QWs of (20.2–46.0) nm width. When analyzing the results, we used self-consistent calculations of the energy spectrum carried out within the framework of the four-band *kP* model.

## II. STRUCTURES INVESTIGATED

Our HgTe quantum wells were realized on the basis of HgTe/Hg$_{1-x}$Cd$_x$Te ($x = 0.5–0.7$) heterostructure grown by molecular beam epitaxy on GaAs substrate of the (013) surface orientation using a CdTe layer (5–7) $\mu$m thick as buffer [17]. The nominal widths of the quantum wells under study were $d = (20.2–46.0)$ nm. The samples were mesa etched into standard Hall bars of 0.5-mm width with the distance between the potential probes of 0.5 mm. To change and control the electron and hole densities ($n$ and $p$, respectively) in the quantum well, the field-effect transistors were fabricated with parylene as an insulator and aluminum as a gate electrode. The measurements were performed in the DC regime of linear response at temperatures (3–20) K in the magnetic field up to 2.5 T. For each heterostructure, several samples were fabricated and studied. The parameters of the structures investigated are presented in Table I.

The main results for all the structures investigated are qualitatively close to each other, therefore, as an example, let us consider in more detail the data obtained for the structure with $d = 32$ nm, for which all the features manifest themselves more clearly.

For a general characterization of the structure, we first analyze the gate voltage dependencies of the electron and hole densities. When $V_g > 1$ V, only electrons participate in the conductivity, the Hall resistance $\rho_{xy}$ at low magnetic field ($B < 0.2–0.4$ T) linearly depends on $B$, and the Hall electron density $n = -1/eR_H$, where $e$ and $R_H$ stand for elementary charge and the Hall coefficient, respectively, increases linearly with the $V_g$ increase [Fig. 1(a)]. When $V_g < 1$ V, the Hall coefficient strongly depends on $B$, changing sign from electronic at low $B$ to holelike with increasing $B$, and at the same time $\rho_{xx}$ increases strongly with $B$ [see inset in Fig. 1(a)]. Within this gate voltage range the electron and hole densities were found by simultaneous fit of dependencies $\rho_{xx}(B)$ and $R_H(B)$ at $B < 0.3$ T within classical model of the conductivity by two types of the carriers. Figure 1(a) shows that total charge

TABLE I. The parameters of heterostructures under study.

| Structure | $d$ (nm) | $n, p$ (cm$^{-2}$)[a] | $\mu_e$ (cm$^2$/Vs)[b] | $n_{sym}$ (cm$^{-2}$) | $n^{(2)}$ (cm$^{-2}$) |
|---|---|---|---|---|---|
| 110614 | 20.2 | $p = 0.8 \times 10^{11}$ | 70000 | $2.0 \times 10^{11}$ | $>7 \times 10^{11}$ |
| 180820 | 22.0 | $n = 4.6 \times 10^{11}$ | 265000 | $3.0 \times 10^{11}$ | $6.3 \times 10^{11}$ |
| 180824 | 32.0 | $p = 0.25 \times 10^{11}$ | 560000 | $1.5 \times 10^{11}$ | $3.6 \times 10^{11}$ |
| 180823 | 46.0 | $p = 0.6 \times 10^{11}$ | 490000 | $0.9 \times 10^{11}$ | $2.9 \times 10^{11}$ |

[a]For $V_g = 0$ V.
[b]For $n = 2 \times 10^{11}$ cm$^{-2}$.

of free carriers in QW $Q = e(p - n)$ linearly depends on $V_g$ as $Q/e = (0.23 - 1.05V_g) \times 10^{11}$, cm$^{-2}$ within whole $V_g$ range. Note that the absolute value of the slope of this dependence $1.05 \times 10^{11}$ cm$^{-2}$ V$^{-1}$ is in a good agreement with that obtained from the capacitance measurements $e\, dn/dV_g = C/S_g$, where $C$ is the capacitance between the 2D gas and the gate electrode, measured for the same structure, $S_g$ is the gated area.

Figure 1(b) shows the electron density dependence of electron mobility at $V_g < 1$ V when electrons exist together with hole (circles) and at $V_g > 1$ V when only electrons contribute to the conductivity (the curve). It is seen that the $n$ dependence of the mobility is nonmonotonic. It increases with $n$ increase while $n \lesssim 3.6 \times 10^{11}$ cm$^{-2}$ and shows a sharp decrease at higher values of $n$ resulting from the beginning of filling the second subband of spatial quantization [see Table I and Fig. 4(b)].

### III. SPIN-ORBIT SPLITTING OF CONDUCTION BAND: EXPERIMENT

The purpose of this paper is to study the spectrum and wave functions of electrons in the conduction band, therefore, below we will discuss the results only for $V_g > 0$. The spectrum of the valence band is much more complicated and should be discussed in a separate paper.

As an example, the magnetic field dependencies of $\rho_{xy}$ and oscillating part of resistivity $\Delta\rho_{xx}(B) = \rho_{xx}(B) - \rho_{xx}^{mon}(B)$, where $\rho_{xx}^{mon}(B)$ is the monotonic part of $\rho_{xx}(B)$, for some gate voltages are presented in Figs. 2(a) and 2(b), respectively. As seen, $\rho_{xy}$ linearly increases with $B$ in low magnetic fields, then the oscillations appear, which are transformed to the steps of the quantum Hall effect in the higher magnetic field. The results of the Fourier transformation of $\Delta\rho_{xx}(1/B)$ performed in the magnetic field range before onset of the steps of the quantum Hall effect are presented in Fig. 2(c).
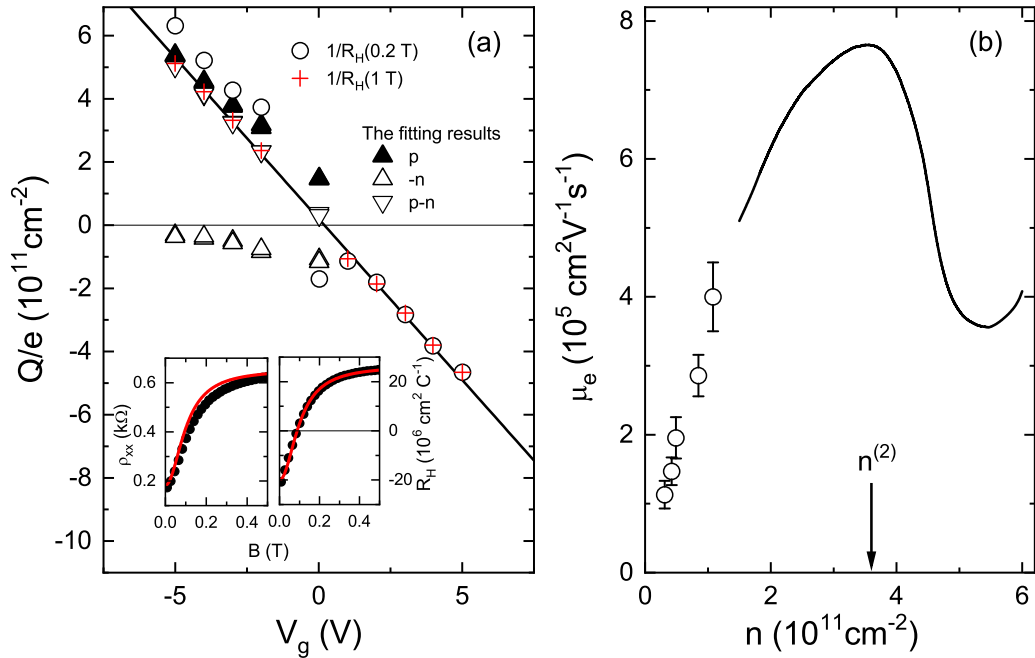


FIG. 1. (a) The gate voltage dependencies of electron and hole charges obtained as $1/R_H(0.2\text{ T})$ ($\circ$), $1/R_H(1.0\text{ T})$ (+) and found from the fit of the data within framework of the two-type carriers model ($\triangle$, $\blacktriangle$). The straight line is the dependence $Q/e = (0.23 - 1.05\,V_g) \times 10^{11}$ cm$^{-2}$. The inset shows an example of the simultaneous fit of dependencies $\rho_{xx}(B)$ and $R_H(B)$ at $V_g = -2$ V within framework of the two-type carriers model. The symbols are the experiment, the curves are the fitting results. (b) The electron density dependence of the electron mobility found from the fit of the experimental dependencies $\rho_{xx}(B)$ and $R_H(B)$ (the circles) and obtained as $-R_H/\rho_{xx}$ at $B = 0.2$ T when $V_g$ is swept (the curve). $T = 4$ K. Structure with $d = 32.0$ nm.
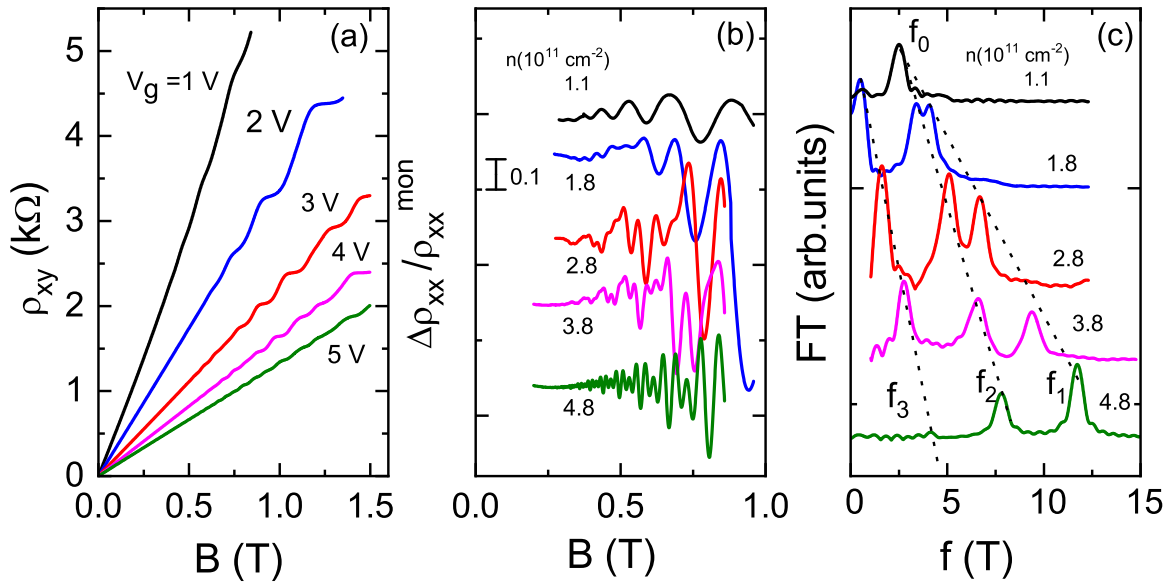
FIG. 2. (a), (b) The magnetic field dependencies of $\rho_{xy}$ and oscillating part of $\rho_{xx}$, respectively. (c) The Fourier spectra of the oscillations shown in (b) performed over the magnetic field range (0.2–0.6) T. Structure with $d = 32.0$ nm.

It is seen that unsplit oscillations with one component in the Fourier spectrum $f_0$ are observed for low-electron density $n \lesssim (1.4–1.5) \times 10^{11}$ cm$^{-2}$. With increasing $V_g$, it splits into two $f_1$ and $f_2$ components, and a low-frequency $f_3$ component appears.

At $n > (1.4–1.5) \times 10^{11}$ cm$^{-2}$, the electron densities found from $f_i$ under assumption of nondegeneracy of electron

states, $n_i = f_i \times e/2\pi\hbar$, are plotted in Fig. 3(a). It can be seen that the sum of the two high-frequency components $f_1 + f_2$ gives a density that coincides with the Hall density. The difference $f_1 - f_2$ coincides with the low-frequency component $f_3$. This is consistent with the following interpretation: (i) the high-frequency components $f_1$ and $f_2$ correspond to two single-spin branches of the first spatially quantized subband
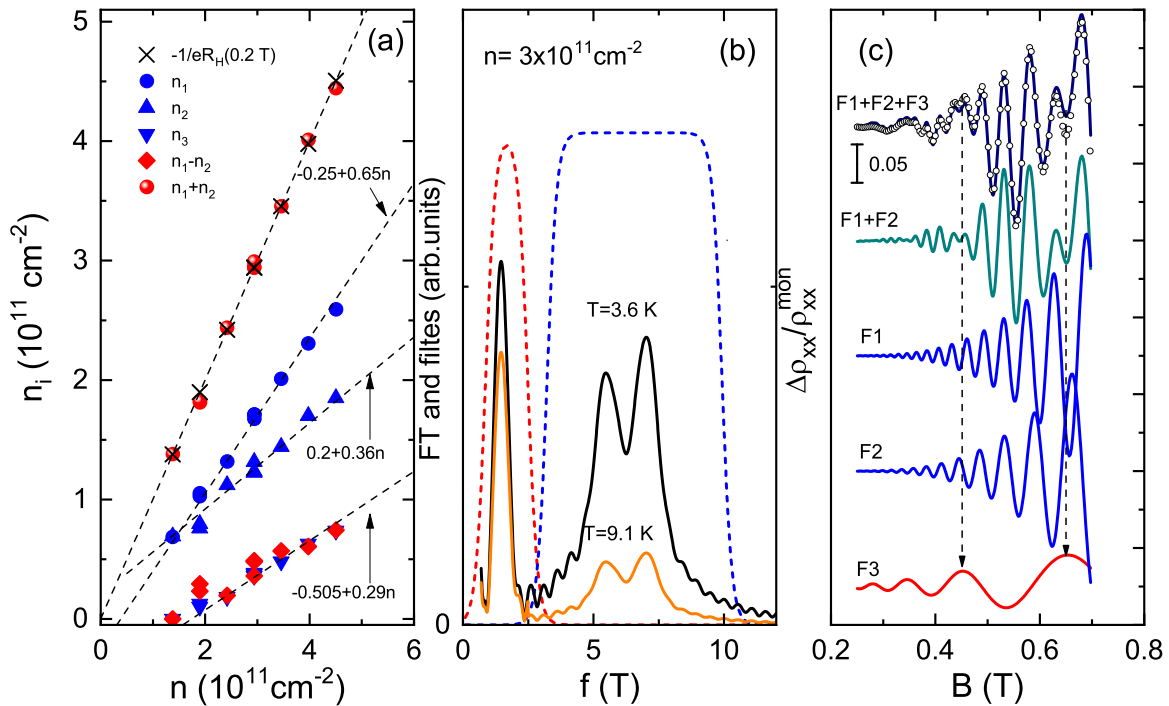


FIG. 3. (a) The density of electrons in the branches, their sum and difference plotted against the total electron density. The straight lines show the results of the linear fit. $T = 3.6$ K. (b) The Fourier spectra of the oscillations at $n = 3 \times 10^{11}$ cm$^{-2}$ for $T = 3.6$ and 9.1 K. The dotted curves show the characteristics of the filters used to separate the low- and high-frequencies components. (c) The oscillating part of resistivity. The points are the experimental dependence. The curves are the results of data analysis (see the text). $T = 3.6$ K. Structure with $d = 32.0$ nm.
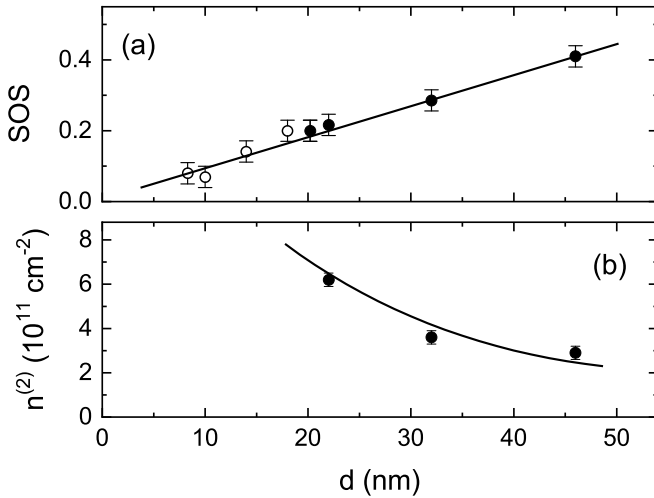
FIG. 4. (a) The SOS value for structures of different width. Solid symbols are the results of this paper, open symbols are the results obtained in Ref. [29]. The curve is a guide for the eye. (b) The density of electrons when the second subband begins to be occupied plotted against the QW width. The symbols are the data, the curve is a guide for the eye.

split due to SO interaction, the splitting value increases with increasing gate voltage; (ii) the low-frequency component $f_3$ arises from the transitions between split branches which result in the well-known magnetointersubband oscillations (MISO). This interpretation is confirmed by the temperature dependence of the amplitudes of these Fourier components shown in Fig. 3(b). It is seen that the amplitude of the two high-frequency components corresponding to the Shubnikov–de Haas (SdH) oscillations of each of the spectrum branches decreases strongly with increasing temperature, while the MISO amplitude decreases insignificantly, as predicted theoretically [44,45].

Figure 3(a) shows that the electron densities in the split branches within experimental uncertainty are well described by the linear dependencies with the different slopes equal to $sl_1 = 0.65$ and $sl_2 = 0.36$. These lines intersect at the point $n \simeq 1.5 \times 10^{11}$ cm$^{-2}$. Therefore, we believe that the quantum well is close to symmetric one at $n_{\mathrm{sym}} \simeq 1.5 \times 10^{11}$ cm$^{-2}$.

To compare the results obtained for the structures with the different QW widths, we will characterize the strength of spin-orbit splitting by the phenomenological parameter SOS $= (sl_1 - sl_2)/(sl_1 + sl_2)$.[1] In Fig. 4(a), we plot the $d$ dependence of SOS for all the structures from Table I and for the structures investigated in Ref. [29]. As seen the SOS value monotonically, without inflection, increases with the increasing QW width over the entire $d$ range. This shows that no new strongly localized surface states arise up to $d = 46$ nm at least.

Another parameter that can be extracted from the analysis of the SdH oscillations is the electron density $n^{(2)}$ at which

the second subband of the spatial quantization begins to be occupied. As seen from Fig. 4(b) the $n^{(2)}$ values diminish with $d$ increase monotonically that as shown in Sec. VI agrees satisfactorily with the theoretical results.

Thus, all the results presented above show that the main magnetotransport properties of wide QWs are qualitatively similar to those previously investigated in QWs with a width of $d < 20$ nm. Their analysis shows that the specific features of the energy spectrum of wide quantum wells are analogous to those of narrower QWs. Namely, the SO splitting is also observed; it increases with the increase of the electron density and with the increase of the QW width.

## IV. ELECTRON MASSES IN THE BRANCHES

By separating the SdH oscillation components corresponding to split branches and analyzing the temperature dependencies of their amplitudes one can obtain the masses in each branch. To separate the components, we used the Fourier spectrum bandpass filtering as shown in Fig. 3(b). To improve the resolution of the Fourier spectra, the oscillating part of $\rho_{xx}(B)$ was multiplied by $1/B$. Then, applying the inverse Fourier transformation we obtained the oscillations of the frequency $f_3$ [the curve F3 in Fig. 3(c)] and superposition of oscillations with two higher frequencies $f_1$ and $f_2$ [the curve labeled as F1+F2 in Fig. 3(c)]. To keep the correct ratio of the amplitudes of the different oscillations, the curves obtained after the inverse Fourier transform were multiplied by $B$. Fitting the curve F1+F2 by the sum of the two Lifshits-Kosevich (LK) formulas [46] allows us to separate the contributions which are presented by the curves F1 and F2 in this figure (for more detail see Ref. [47]). This method of decomposition allows us not only to reliably separate out the contributions of each of the three oscillation components and determine their frequencies, but also to determine the amplitudes. Applying this procedure to analyze the oscillations measured for different temperatures one can obtain the temperature dependencies of the amplitudes of the oscillations coming from the branches and hence obtain the cyclotron effective mass $m = \hbar^2 k (dE/dk)^{-1}$ at the Fermi energy for each of the branches.

The inset in Fig. 5 shows the temperature dependencies of the amplitudes of the SdH oscillation components for $B = 0.5$ T separated as described above for the total electron density $n = 3.3 \times 10^{11}$ cm$^{-2}$. It is seen that the temperature dependencies of the amplitudes are very close to each other. They are well fitted by the LK formula that gives the values of effective masses $m = (0.0258 \pm 0.0015)m_0$ and $(0.0242 \pm 0.0015)m_0$ for the electron densities in the branches equal to $1.9 \times 10^{11}$ cm$^{-2}$ and $1.42 \times 10^{11}$ cm$^{-2}$, respectively. These values and the values obtained for the other electron densities are shown in Fig. 5 by squares and triangles. As seen the effective masses in the split branches are very close to each other.

We attract here the reader's attention to a peculiarity of MISO in HgTe-based QWs already discussed in Ref. [47] for the narrower quantum wells. Figure 3(c) shows that beating of the SdH oscillations results as a sum of two high-frequency components. As seen, the magnetic fields of the antinodes of high-frequency oscillations correspond to the minima in

---

[1]This is of course an approximation. In the paper [29] we show that the theory predicts nonlinear dependencies $n_1(V_g)$ and $n_2(V_g)$ at the small splitting values. However, in order to trace the change in spin-orbit splitting with the $d$ change, such a SOS parameter is suitable.
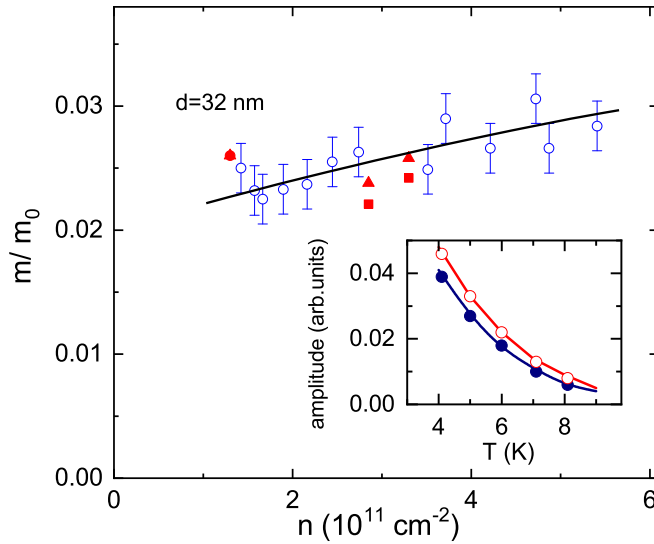
FIG. 5. The electron density dependence of the electron effective mass at the Fermi energy for the structure with $d = 32.0$ nm. The triangles and squares are the masses in each of the branches of the spectrum obtained from the temperature dependencies of the amplitudes of the separate SdH oscillation components of $\rho_{xx}(B)$. The circles are the average value of the masses in the branches obtained from the temperature dependence of the oscillation amplitude of $d^2\rho_{xx}/dV_g^2$ measured with a change in the gate voltage at $B = 0.5$ T. The line is a guide for the eye. The inset shows the temperature dependencies of the amplitudes of separate components of the SdH oscillations at $B = 0.5$ T for $n = 3.3 \times 10^{11}$ cm$^{-2}$. The symbols are the data, the lines are the results of the best fit to the LK formula.

$\rho_{xx}$-MISO. Such a mutual position is opposite to that observed in ordinary structures, namely, in double and wide quantum wells. But it agrees with that observed in narrow HgTe- and In$_x$Ga$_{1-x}$As-based QWs, in which the splitting of oscillation arises due to spin-orbit splitting. The authors of Ref. [47] assume that the unusual mutual positions of the MISO extrema and the SdH oscillation antinodes originate from the dependence of the probability of transitions between the Landau levels of different branches on the difference in their energies.

Let us consider the data obtained by the other method which gives the effective mass over a wide electron density range. It consists in analyzing the temperature dependence of the amplitude of the oscillations of the $d^2\rho_{xx}/dV_g^2$ vs $V_g$ dependencies in a fixed magnetic field. This method gives an average of the effective masses in the branches. The results are shown in Fig. 5 by circles. It is seen that the results obtained by the two methods practically coincide. The effective masses increase slightly with an increase in the total electron concentration from $(0.020 \pm 0.003)m_0$ at $n = 1.5 \times 10^{11}$ cm$^{-2}$ to $(0.030 \pm 0.003)m_0$ at $n = 4.5 \times 10^{11}$ cm$^{-2}$.

The same measurements and analyses were carried out for all the structures under study. The results are shown in Fig. 6. It is seen that effective masses of QWs with $d = (22.0–46.0)$ nm are close to each other over the whole electron density range. They are within the shadow area which width is comparable with the experimental errors. In the same figure, we plot the theoretical dependencies calculated within the framework of the standard $kP$ model for the rectangular quantum well
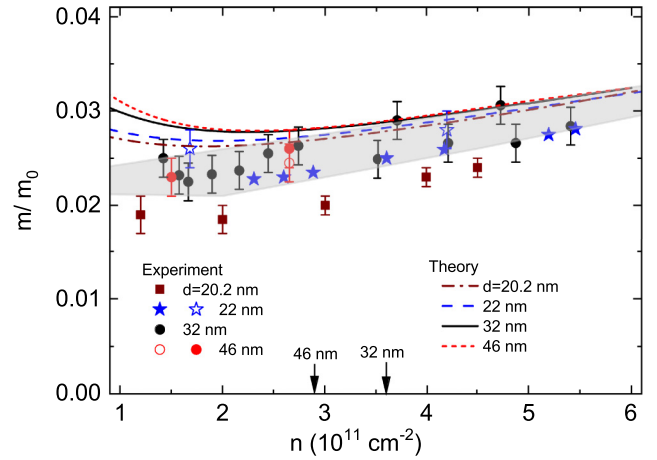


FIG. 6. The electron density dependence of the electron effective mass for the structures with different QW width. The symbols are the data, the lines are the calculated dependencies for rectangular quantum well. The shadow area is the area within which the experimental data for QWs with $d = (22.0–46.0)$ nm are. The arrows show the $n^{(2)}$ values for $d = 32.0$ and 46.0 nm.

when the potential of electric charge is not taken into account. It is seen that the theoretical dependencies and experimental plot are qualitatively similar. As for the data point for the QW with $d = 20.2$ nm, the low values of the effective mass in the narrow QWs, $d = (7–20)$ nm, are already observed and discussed earlier [2]. Thus, the above measurements show that the effective masses of electrons in the split branches are close to each other. In addition, the values of $m_e$ and their dependence on the electron concentration are similar for all structures studied.

Let us now consider the behavior of MISO with changing the electron density in QWs of different widths.

## V. MISO AMPLITUDE WITH CHANGING ELECTRON DENSITY AND QW WIDTH

The Fourier spectra of the oscillating part of $\rho_{xx}(B)$ for three structures for some electron densities are presented in Fig. 7 (in contrast to Fig. 3, the Fourier transformation was performed here without correcting the dependence of the amplitude of oscillations on the magnetic field). Let us first compare the strength of MISO and SdH oscillations qualitatively. At first glance, the ratio of the amplitude of the Fourier peaks of MISO and SdH oscillations is approximately the same in structures with different QW widths. Seemingly, it contradicts to intuitive expectations and theoretical predictions according to which the overlapping of the wave functions of two branches should decrease with the increasing QW width that should result in decrease of the probability of transitions between them, and, consequently, to a decrease in the MISO amplitude.

It would seem that by separating the oscillations, we find both prefactors and exponentials that describe the dependence of the oscillations on the magnetic field, and then one should compare these parameters for the SdH oscillations and MISO. However, our analysis shows that each of these parameters is found with not enough accuracy, only their combination is
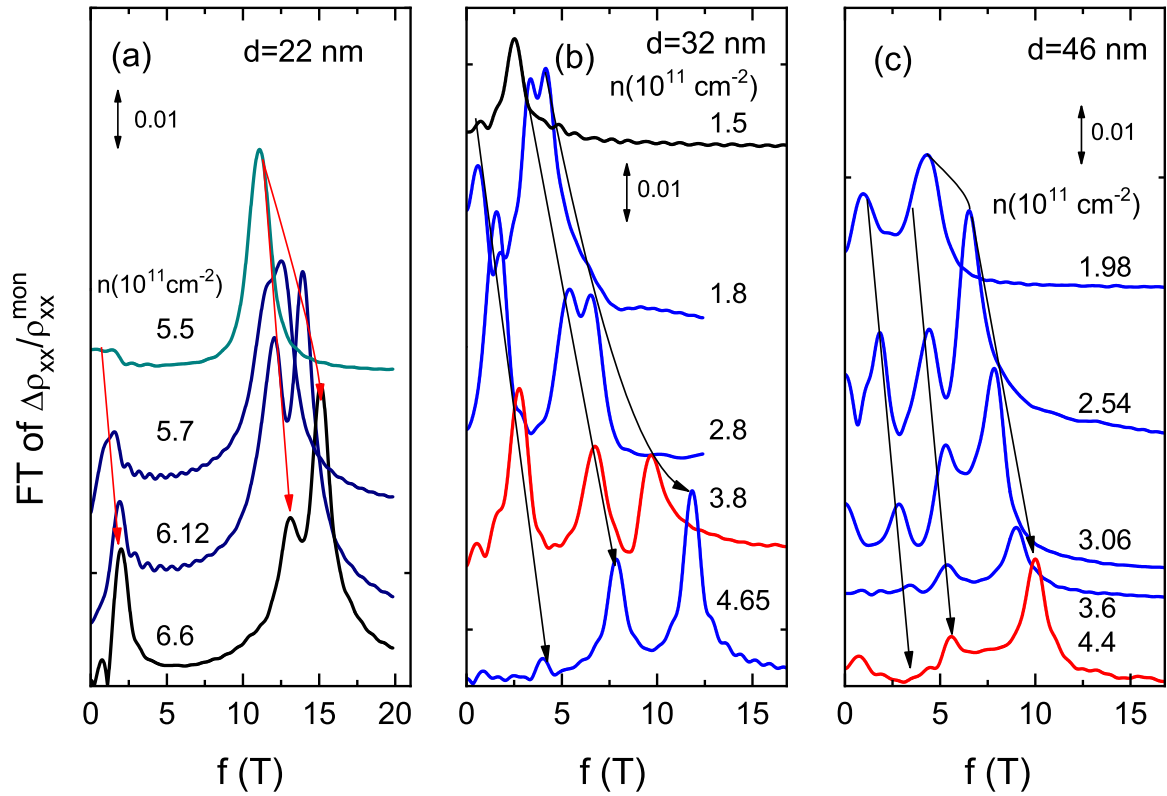
FIG. 7. The Fourier spectra of $\Delta\rho_{xx}/\rho_{xx}^{mon}$ for structures investigated. The Fourier transformation was performed without correcting the dependence of the amplitude of oscillations on the magnetic field as has been done for Fig. 3. For clarity, the curves are shifted along the vertical axis. $T = 3.6$ K.

obtained well. Therefore, we restrict ourselves to comparing the areas under the Fourier peaks of the spectra corresponding to MISO and SdH oscillations, denoted as $S_{MISO}$ and $S_{SdH}$, respectively. The $S_{MISO}/S_{SdH}$ values plotted against $n - n_{sym}$ are shown in Fig. 8.

It is seen that for a small splitting, that corresponds to $n - n_{sym} \lesssim 1 \times 10^{11}$ cm$^{-2}$, the ratio $S_{MISO}/S_{SdH}$ does not change much with increasing $d$, although the overlap of the
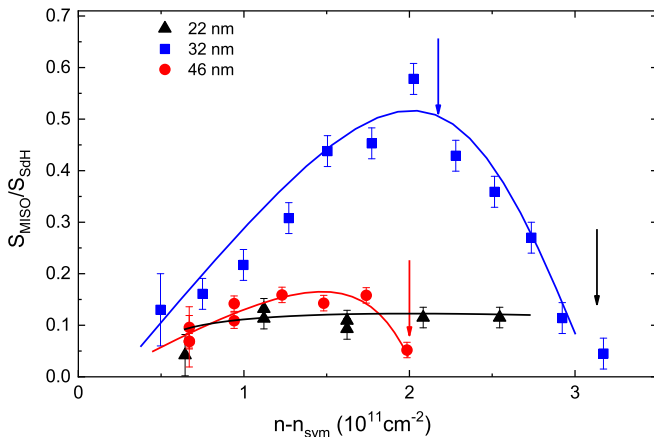


FIG. 8. The $S_{MISO}/S_{SdH}$ values plotted as a function of $n - n_{sym}$. The lines are a guide to the eye. The arrows show the densities at which the second subbands begin to be occupied.

wave functions of different branches should seem to decrease strongly.

Most important in Fig. 8 in our opinion is the difference in the dependencies of $S_{MISO}/S_{SdH}$ on $n - n_{sym}$. As seen the ratio $S_{MISO}/S_{SdH}$ for QW with $d = 22.0$ nm does not depend on the density within the experimental accuracy. In QWs with $d = 32.0$ and 46.0 nm, the $S_{MISO}/S_{SdH}$ value noticeably increases with an increase of $n - n_{sym}$. Such a behavior seems strange because with an increase of electron density (i.e., with an increase of the Fermi quasimomentum) the overlapping of the wave functions of two branches located at different QW walls decreases at least in the empty spectrum [see Fig. 9(b)]. Figure 8 also shows sharp drops in $S_{MISO}/S_{SdH}$ at $(n - n_{sym}) \simeq 3 \times 10^{11}$ and $1.6 \times 10^{11}$ cm$^{-2}$ for structures with $d = 32$ and 46 nm, respectively. These electron densities are close to the beginning of the filling of the second subband of spatial quantization [see Table I, and Figs. 1(b) and 4(b)].

Thus, we observe the MISO in all the structures. The MISO amplitude exhibits an unexpected, counterintuitive behavior with increasing electron concentration. It grows with increasing $n - n_{sym}$. This growth turns into a sharp decrease when the second subband of spatial quantization begins to be occupied with a further $n$ increase.

In order to understand and interpret all the results presented above, namely, the electron density dependencies of the splitting magnitude, masses in the branches, MISO amplitude in the quantum wells of different widths, let us consider the predictions of the $kP$ theory.
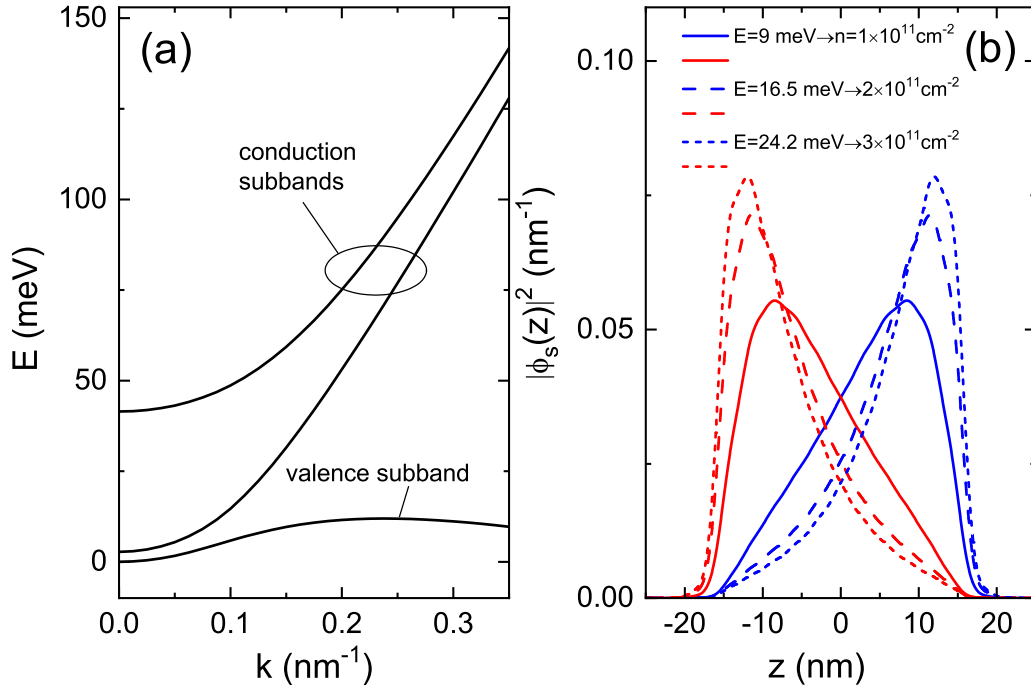
FIG. 9. (a) The energy spectrum of the rectangular QW of 32-nm width. (b) $|\phi_s(z)|^2$ for two states of the conduction band at different energies corresponding to the different electron densities.

## VI. RESULTS OF CALCULATION: THE ENERGY SPECTRUM AND WAVE FUNCTIONS

The energy spectrum for the HgTe-based QWs was calculated using the Kane's four-band model including second-order remote band contributions. The expression for the $8 \times 8$ Hamiltonian of the heterostructure grown on the plane of different orientations was derived by the method described in Refs. [48,49]. The components of the built-in strain tensor were calculated with the use of the formulas from [5]. Parameters to describe the deformation contribution to the Hamiltonian were taken from Ref. [50]. To take into account the interface inversion asymmetry we used an additional term in the Hamiltonian, which is suggested by Ivchenko [51] (see also Ref. [27] for more details).

To account for the influence of the electrons on the electric field distribution across the quantum well, the standard self-consistent procedure of simultaneous solution of the Schrödinger equation and Poisson equation

$$\frac{d}{dz}\left(\kappa(z)\frac{d}{dz}\varphi(z)\right) = \frac{e}{(2\pi)^2}\sum_s \int d^2\mathbf{k}|\Psi_s(\mathbf{k})|^2 f[\varepsilon_s(\mathbf{k})]$$
$$- \frac{eN_D^+}{d} \qquad (1)$$

was used. Here, $\kappa(z)$ is the dielectric susceptibility, $\varphi(z)$ is the electrostatic potential, $f[\varepsilon_s(\mathbf{k})]$ is the Fermi-Dirac distribution function, $\Psi_s(\mathbf{k})$ is the wave function of eight components, which has the form

$$\Psi_s(\mathbf{k}) = C_s \exp(ik_x x + ik_y y)\phi_s(z, k_x, k_y), \qquad (2)$$

$N_D^+$ is the density of charged donors (it is supposed that the donors are distributed uniformly across the quantum

well[2] and their density is equal to the electron density at the gate voltage for which the quantum well is symmetric $N_D^+ = n_{\text{sym}}$), the summation in Eq. (1) runs over the spatial quantization subband including the "spin" index. To solve the Schrödinger equation we set the boundary conditions on the planes $z = \pm z_0$ assuming that the center of the quantum well was located at $z = 0$. The value of $z_0$ was chosen in such a way that the wave functions at $z = \pm z_0$ were practically equal to zero. Usually, it was enough for the value of $z_0$ to exceed the width of the quantum well by 40 nm. Equation (1) was solved with the following boundary conditions:

$$\varphi(-z_0) = 0,$$
$$\left.\frac{d\varphi(z)}{dz}\right|_{z=-z_0} = 0, \qquad (3)$$

where is assumed that the gate electrode is located at positive $z$.

To calculate the energy spectrum and wave functions for a given $n$ value, we solved simultaneously the Schrödinger and Poisson equations by using an iterative method. First, the electron spectrum is calculated for zero potential. The wave functions obtained are used to calculate the electron charge distribution corresponding to given $n$. This distribution is substituted in the right-hand side of the Poisson equation (1). Obtained $\varphi(z)$ is substituted in the Hamiltonian and then the Schrödinger equation is solved again. The procedure is repeated until the potential $\varphi(z)$ converges. This usually requires 5–10 iterations.

---

[2]It should be mentioned that the results under consideration are practically insensitive to where the donors are located: in the quantum well or in the barriers.
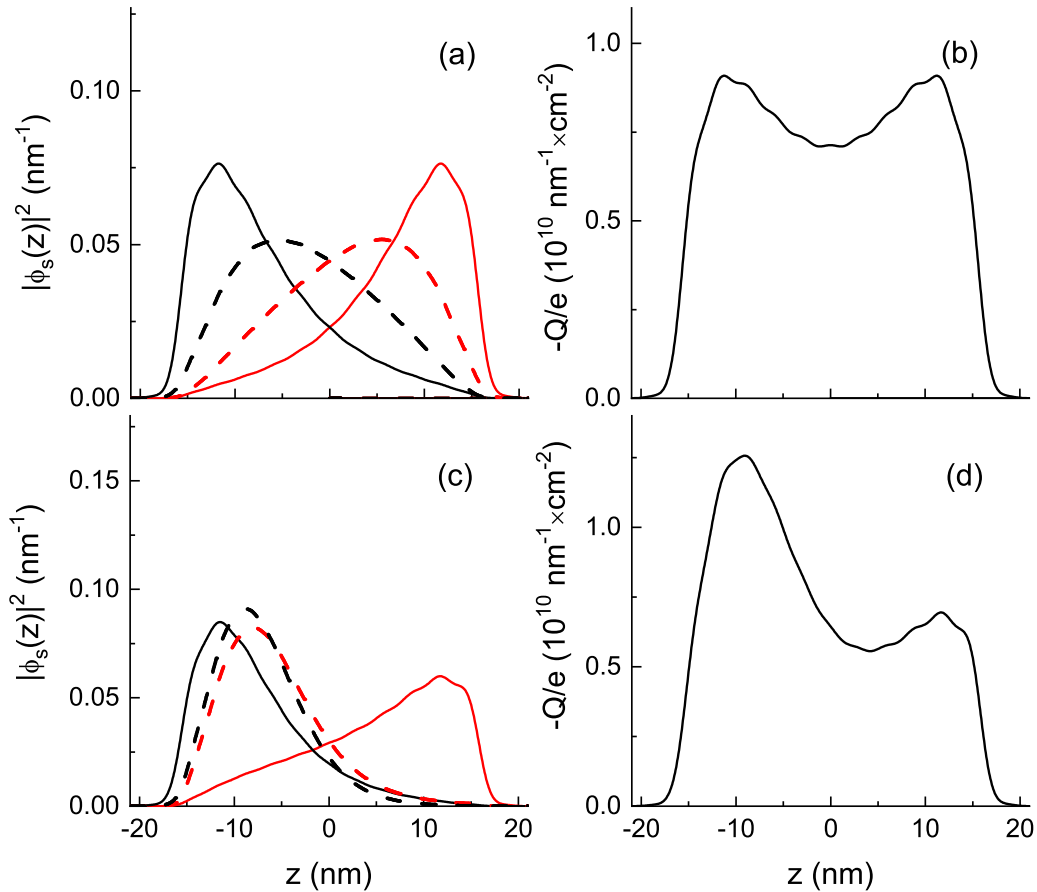
FIG. 10. (a), (c) The dependence $|\phi_s(z, k_F^{(s)})|^2$ for two states $s = 1, 2$ at $k_F^{(s)}$ (solid lines) and $0.5\, k_F^{(s)}$ (dashed lines). (b), (d) The distribution of electric charge. The $k_F$ value corresponds to the electron density $2.5 \times 10^{11}$ cm$^{-2}$. The panels (a), (b) and (c), (d) show the calculation results obtained without and with applying the self-consistent procedure, respectively. $d = 32$ nm.

The other theoretical details, including the Hamiltonian in the explicit form, the calculation method, and the parameters used, can be found in the Supplemental Material [52].

Let us first consider the calculation results for the empty spectrum, i.e., when QW is rectangular in the shape. The dispersion $E(k)$ is depicted in Fig. 9(a), while the normalized sum of squares of eight components of wave functions for two states of the conduction band $|\phi_s(z)|^2$, $s = 1, 2$, for QW with $d = 32.0$ nm are shown in Fig. 9(b). As seen from Fig. 9(b) the wave functions of each of the branches are localized near one of the QW wall, and the larger the $k$ value the stronger the localization and the less the overlap of the wave functions of different branches. An approach of the empty spectrum is, however, inapplicable to describe the experiment. This is because the charge distribution changes and, hence, the shape of the quantum well also changes when the electron density is tuned via the voltage on the gate electrode. Self-consistent procedure should be used for that.

An importance of the role of the potential of electrons in the forming shape of the quantum well is illustrated by Fig. 10. The dependencies $|\phi_s(z)|^2$ for $k_F^{(s)}$ (dashed lines) and $0.5\, k_F^{(s)}$ (solid lines) for two states, $s = 1, 2$, for $k_F^{(s)}$ corresponding to the electron density $2.5 \times 10^{11}$ cm$^{-2}$ before self-consistency are shown in Fig. 10(a). The distribution of electron charge $Q(z)$ is presented in Fig. 10(b). As evident from the last

figure $Q(z)$ is symmetric and the average value of the electron charge position is equal to zero for this case. The same
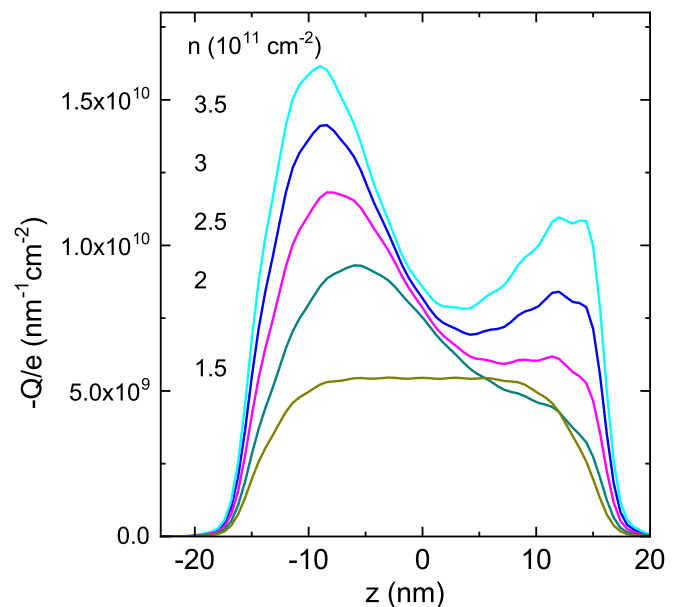


FIG. 11. The redistribution of the charge in QW with increasing electron density caused by $V_g$ increase. $d = 32.0$ nm.
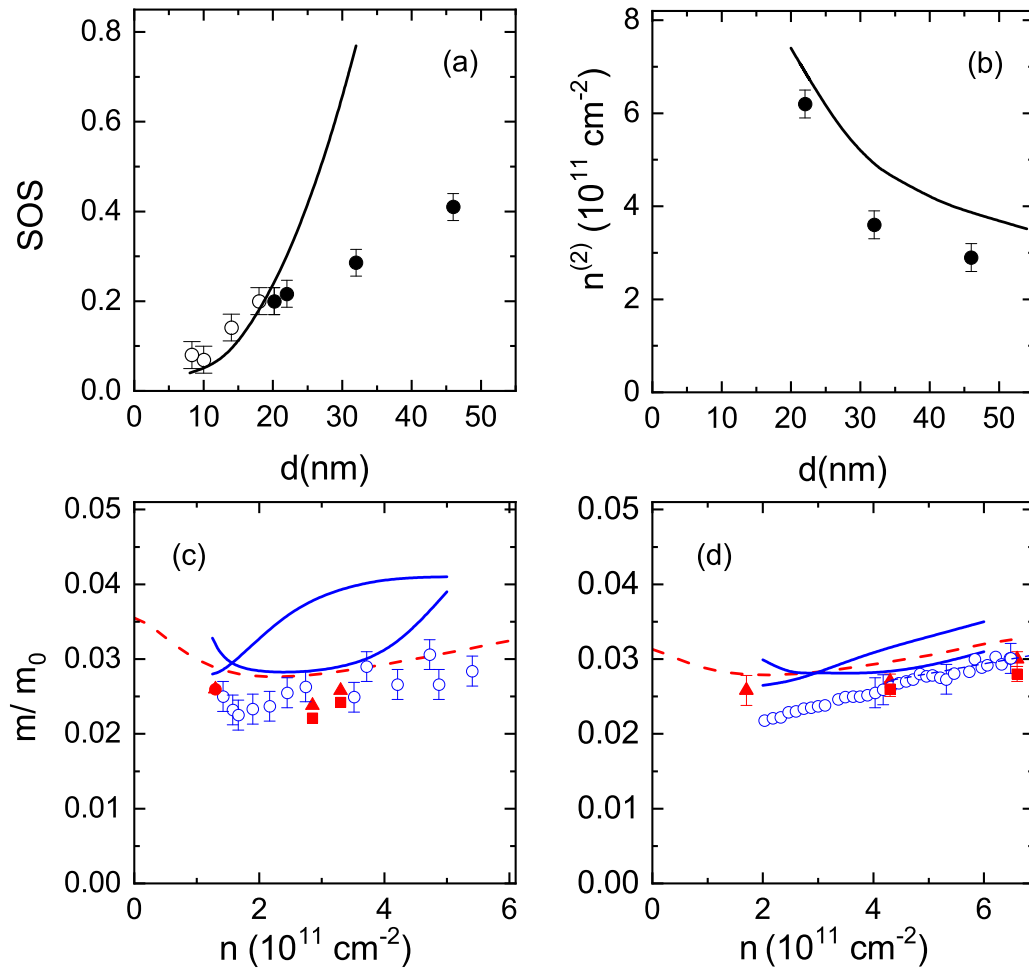
FIG. 12. (a) The SOS value for QWs of different widths. The symbols are the data from Fig. 4(a). The curve is result of self-consistent calculation. (b) The density of electrons when the second subband begins to be occupied. The symbols are the data from Fig. 4(b), the line is result of self-consistent calculation. (c), (d) The electron density dependence of the electron effective mass at the Fermi energy for the structures with $d = 32$ and 22 nm, respectively. The triangles and squares are obtained from the temperature dependencies of the amplitudes of the separated SdH oscillations $\rho_{xx}(B)$ and correspond to the masses in each of the branches of the spectrum. The circles are obtained from the temperature dependence of the oscillation amplitude of $d^2\rho_{xx}/dV_g^2$, measured with a change in the gate voltage at $B = 0.5$ T, and correspond to the average value of the masses in the branches. The dashed lines are calculated for the rectangular QW. The solid lines are the result of a self-consistent calculation of masses for each branch.

dependencies after procedure of self-consistency are shown in Figs. 10(c) and 10(d). It is clearly seen that both $|\phi_s(z)|^2$ and $Q(z)$ are modified drastically.

Redistribution of the electron charge in QW with the growing gate voltage inducing the electron density increase is shown in Fig. 11. As seen, the charge shifts monotonically away from the gate electrode with an increase in the positive charge on it, first quickly, then slowly. The center of gravity of the charge distribution shifts away from the gate, which corresponds to the repulsion of the electronic state from the gate electrode charged positively. Such a behavior is counterintuitive and corresponds to negative polarizability (this phenomenon for analogous structures was discussed in Ref. [53]).

Now we are in position to compare the results of self-consistent calculations with our experimental data (see Fig. 12). Let us first consider the dependence of SOS on the QW width. As seen from Fig. 12(a) both the experi-

mental and calculated dependencies grow with increasing $d$, and for $d < 22$ nm the theoretical dependence describes the experiment well. However, at $d > (22–25)$ nm, the calculated dependence increases much faster. The calculated and experimental dependencies $n^{(2)}(d)$ are in a rather good agreement [see Fig. 12(b)].

The comparison between the experimental and calculated effective masses is given in Figs. 12(c) and 12(d) for $d = 32$ and 22 nm, respectively. As seen, the calculated effective masses are different for the split branches that qualitatively agree with the data. However, quantitatively, this difference is much less experimentally. The other point is that the experimental masses are less as compared with the calculated ones practically for all the electron densities. As already mentioned above, the last discrepancy for HgTe-based QWs is discussed earlier in Ref. [2] where assumption was made that such a behavior may result from the many-body effects.
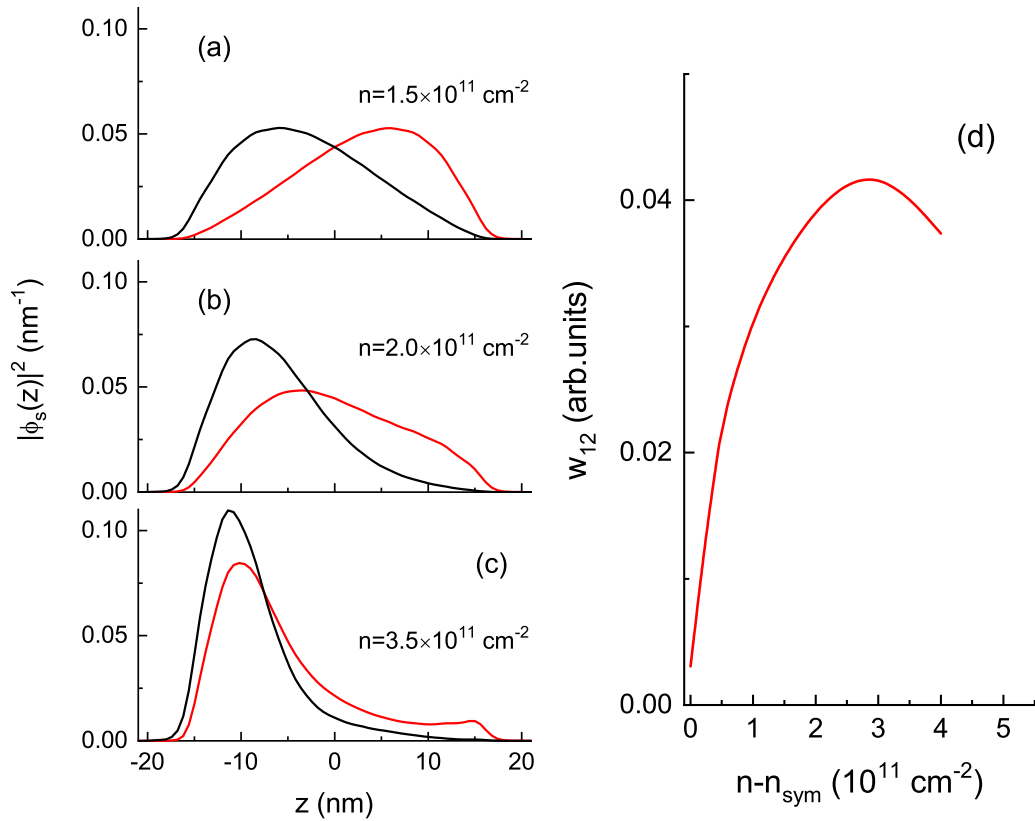
FIG. 13. (a)–(c) The transformation of the probability density distribution $|\phi_s(z)|^2$ at $k_F^{(s)}$ with growing electron density controlled by the gate voltage. (d) The rate of the $k_F^{(1)} \rightarrow k_F^{(2)}$ transitions due to scattering on the short-range random potential plotted against $n - n_{\text{sym}}$. $d = 32.0$ nm.

The theoretical model used provides also qualitative understanding of the unusual behavior of the MISO amplitude with growing electron density considered in Sec. V. As Figs. 13(a)–13(c) illustrate the growing gate voltage results to the strengthening overlap of wave functions of the branches due to their displacement away from the gate electrode that in its turn leads to strong increase of the rate of the transitions between different spin states $w_{12}$ [Fig. 13(d)].

Thus, the results of self-consistent calculations of the electron energy spectrum and wave functions agree with the experimental results concerning to SOS and $m_e$ qualitatively. An important result of the calculations is that the electron wave functions are significantly shifted along $z$ direction with the changing gate voltage which controls the density of electron in the QW. They move away from the gate electrode with an increase of the positive charge on it. This corresponds to the negative polarizability of electrons and makes it possible to qualitatively understand the increase in the MISO amplitude with increasing $n - n_{\text{sym}}$.

The charge redistribution over $z$ direction with the varying gate voltage discussed above should manifest itself in the $V_g$ dependence of the capacitance between the QW and gate electrode.

## VII. RESULTS OF CAPACITANCE MEASUREMENTS

The gate voltage dependence of capacitance between 2D gas and the gate electrode results from the finite density of states of a 2D gas and it can be written as

$$C^{-1} = C_g^{-1} + C_q^{-1}, \quad C_q = e^2 D, \qquad (4)$$

where $C_g$ is geometrical capacitance, and $D$ is the density of states of 2D gas which is related to the effective mass of the carriers at the Fermi level as $D = m/(\pi \hbar^2)$.

The samples under study differ slightly (by 20%) in dielectric thickness, gate area, and $V_g$ value corresponding to the charge neutrality point, therefore, the results of the volt-capacitance measurements obtained for the different structures are shown in Fig. 14(a) as $C/C_g$ vs $Q/e$ plot.

To determine $C_g$, we used the fact that the measurements of the Hall density and SdH oscillations at different $V_g$ and $T$ in the hole region showed that (i) the degeneracy of the states of valence band top is equal to two up to the hole density $(4–5) \times 10^{11}$ cm$^{-2}$; (ii) the effective mass of holes is large, and its value is close to each other for all the structures and equal to $m_h = (0.25 \pm 0.05)m_0$. With taking this into account the $C_g$ value can be obtained as $C_g = (1/C - 1/C_q^{\text{holes}})^{-1}$, where $C$ is the experimental capacity measured within the hole region at $p = (2–3) \times 10^{11}$ cm$^{-2}$, $C_q^{\text{holes}} = e^2 m_h/(\pi \hbar^2)$ is the hole quantum capacity.

Figure 14(a) shows that the capacitance drops sharply at $n = (0.5–1.0) \times 10^{11}$ cm$^{-2}$ and has a minimum at the nonzero electron densities $n = (1.9–2.5) \times 10^{11}$ cm$^{-2}$. This is due to two factors: (i) at these QW widths, the conduction and valence bands overlap; (ii) the effective mass of holes is much (about 10 times) larger than that of the electrons. In
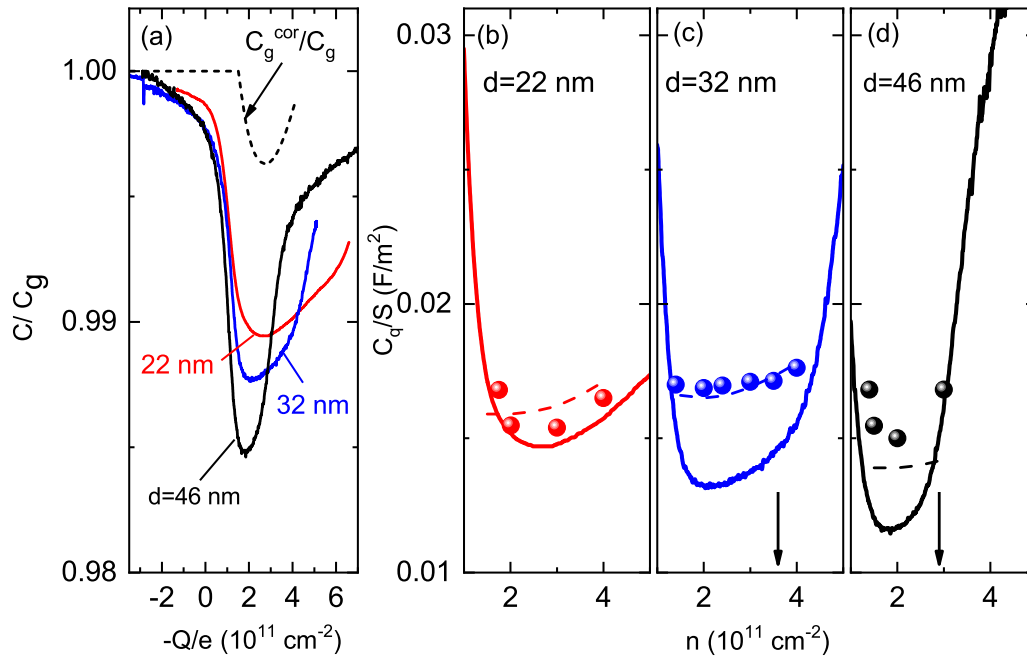
FIG. 14. (a) The dependence of $C/C_g$ on the charge of the free carriers for different QWs. The dashed curve is an example for QW with $d = 32$ nm of the corrected geometrical capacity which provides the coincidence of the quantum capacity found from the experimental dependence $C(V_g)$ [the dashed line in (c)] with that obtained from the density of states with use of the experimental effective mass [the balls in (c)]. (b)–(d) The solid lines are the quantum capacity $C_q/S$ obtained as described in the text with $C_g = $ const. The balls are the $C_q/S$ values calculated with $m$ value measured on the same structures (see Fig. 6). The dashed lines are $C_q/S$ obtained with taking into account the $V_g$ dependence of the geometrical capacity. The arrows show the electron density at which the second subband of spatial quantization starts to be occupied.

ordinary structures, the drop is associated with a decrease in the density of states and, therefore, with a large contribution of the quantum capacitance. The values of quantum capacity $C_q/S$ calculated from these dependencies with a fixed geometric capacity are shown in Figs. 14(b)–14(d). It is seen that the $C_q/S$ value at the minimum decreases with an increase in the QW width, which seems to correspond to a smaller value of the electron mass in wider QWs. However, this contradicts the experimental results on the electron masses obtained from the analysis of SdH oscillations shown in Fig. 6.

In order to understand what the seemingly smaller value of the electron mass found from $C(V_g)$ can be connected with, let us consider what approximations were made when obtaining the formula (4). It was tacitly assumed that the charge distribution in QW over $z$ axis does not change with a change in the density of charge carriers by the gate voltage. Recall that self-consistent calculations (see Figs. 10 and 11) show that $V_g$ changes the charge distribution in the $z$ direction. In our case, as discussed above, electrons are repulsed from the gate electrode at a positive voltage that can be considered as the change (decrease in the given case) of the geometrical capacity.

Using this simple model one can easily find how the geometrical capacity $C_g^{\text{cor}}$ should depend on the gate voltage so that $C_q$ calculated from Eq. (4) with replacement of $C_g$ by $C_g^{\text{cor}}$ coincides with $C_q$ calculated from the density of states with the use of the experimental effective mass. The results for $C_g^{\text{cor}}(V_g)$ for the structures with $d = 32$ nm are shown in Fig. 14(a) by the dashed line. As Figs. 14(a) and 14(c) illustrate, the decrease of the geometrical capacity by the

value of 0.3% in the minimum for structure with $d = 32$ nm gives good agreement between $C_q$ values calculated from the experimental effective mass and found from the $C$ vs $V_g$ measurements. The simple estimate with the use of the formula of the flat capacitor gives that this decrease in the geometrical capacitance corresponds to increase of the distance between the capacitor plates, i.e., to the shift of the electron density
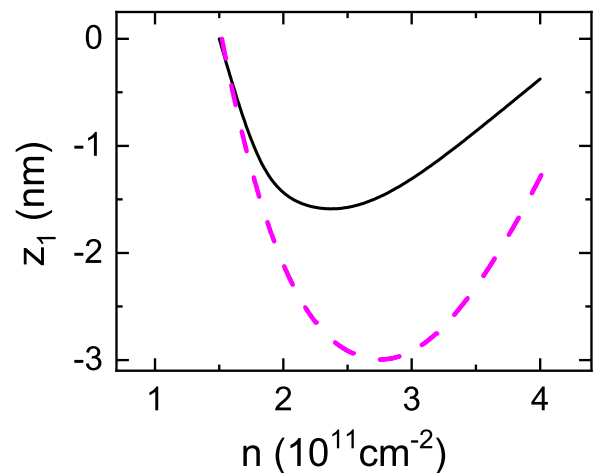


FIG. 15. The solid line is the calculated electron density dependence of the center of gravity of the electron charge distribution $z_1$ for the structure with $d = 32$ nm. The dashed line is obtained from $C_g^{\text{cor}}$ vs $Q/e$ dependence shown in Fig. 14(a) with the use of the formula of the flat capacitor.

away from the gate electrode, by the value of about 3 nm (Fig. 15). This simple consideration agrees qualitatively with the results of theoretical calculations. This is illustrated by the same figure in which we also show the calculated electron density dependence of the position of the center of gravity of the electron charge distribution ($z_1$) relative to the QW center.

Thus, interpreting the experimental gate voltage dependencies of the capacitance between the 2D electron gas and the gate electrode we have estimated the magnitude of the shift of the charge in the quantum well along the $z$ direction and the change in the overlap of the wave functions with a $V_g$ change. These results confirm the interpretation of the unexpected increase in the MISO amplitude presented in Sec. V.

## VIII. CONCLUSION

We have experimentally studied the magnetotransport and capacitance between 2D gas and the gate electrode in HgTe-based quantum wells of (20–46) nm width. It is shown that an increase in the electron density controlled by the gate voltage leads to a spin-orbit splitting of the Bychkov-Rashba type of the conduction band spectrum. This splitting drastically increases with the increasing QW width so that the ratio of the electron densities in the split branches achieves the value of about 2.5–3.0 in QW with $d = 46$ nm at the electron density of $(3.0–3.5) \times 10^{11}$ cm$^{-2}$.

As the width of the well increases, the electron density at which the second subband of spatial quantization begins to be occupied decreases and the electron effective mass and its electron density dependence, as expected, are practically independent of the QW width.

In the entire range of the QW widths, the magnetointer-subband oscillations (MISO) are observed, which indicates that the overlap of wave functions of different branches is sufficiently large even in the widest QW with $d = 46$ nm. In addition, the electron density dependence of the MISO amplitude is unexpected. The amplitude increases with the increasing electron density, while simple calculations predict a decrease in overlap with energy increase.

The data obtained were interpreted using the self-consistent calculation of the energy spectrum within the framework of the four-band $kP$ model. Theoretically, the wave functions demonstrate a shift across the quantum well corresponding to the negative electron polarizability with an increase of the gate voltage. Such a shift leads to an increase in the overlap of the wave functions of different branches and, as a consequence, to an increase in the rate of transitions, and hence to an increase in the MISO amplitude. It is shown that this shift also manifests itself in the gate voltage dependence of the capacitance measured between the gate electrode and the quantum well.

Analyzing the data we conclude that standard self-consistent calculations are only in qualitative agreement with the experimental results. A possible reason is the difference of dielectric susceptibility of the layer forming the quantum well from that of the parent bulk material as discussed in Refs. [39,43,54,55]. We are not aware of papers in which this was considered for such a complicated spectrum as HgTe/Hg$_{1-x}$Cd$_x$Te QWs. Further theoretical studies are needed to understand which effects are not taken into account yet in order to describe the data quantitatively.

[1] S. Groves and W. Paul, Band Structure of Gray Tin, Phys. Rev. Lett. **11**, 194 (1963).

[2] G. Minkov, V. Y. Aleshkin, O. Rut, A. Sherstobitov, A. V. Germanenko, S. Dvoretski, and N. Mikhailov, Electron mass in a hgte quantum well: Experiment versus theory, Physica E (Amsterdam) **116**, 113742 (2020).

[3] L. G. Gerchikov and A. Subashiev, Interface states in subbabnd structure of semiconductor quantum well, Phys. Status Solidi B **160**, 443 (1990).

[4] X. C. Zhang, A. Pfeuffer-Jeschke, K. Ortner, V. Hock, H. Buhmann, C. R. Becker, and G. Landwehr, Rashba splitting in $n$-type modulation-doped hgte quantum wells with an inverted band structure, Phys. Rev. B **63**, 245305 (2001).

[5] E. G. Novik, A. Pfeuffer-Jeschke, T. Jungwirth, V. Latussek, C. R. Becker, G. Landwehr, H. Buhmann, and L. W. Molenkamp, Band structure of semimagnetic Hg$_{1-y}$Mn$_y$Te quantum wells, Phys. Rev. B **72**, 035321 (2005).

[6] B. A. Bernevig, T. L. Hughes, and S.-C. Zhang, Quantum spin hall effect and topological phase transition in hgte quantum wells, Science **314**, 1757 (2006).

[7] M. Zholudev, Ph.D. thesis, University Montpellier 2, France, 2013.

[8] Y. Ren, Z. Qiao, and Q. Niu, Topological phases in two-dimensional materials: A review, Rep. Prog. Phys. **79**, 066501 (2016).

[9] M. I. D'yakonov and A. Khaetskii, Zh. Eksp. Teor. Fiz. **82**, 1584 (1982) [Sov. Phys.–JETP **55**, 917 (1982)].

[10] Z. D. Kvon, E. Olshanetsky, D. A. Kozlov, N. N. Mikhailov, and S. A. Dvoretskii, Pis'ma Zh. Eksp. Teor. Fiz. **87**, 588 (2008) [JETP Lett. **87**, 502 (2008)].

[11] Z. D. Kvon, E. B. Olshanetsky, E. G. Novik, D. A. Kozlov, N. N. Mikhailov, I. O. Parm, and S. A. Dvoretsky, Two-dimensional electron-hole system in hgte-based quantum wells with surface orientation (112), Phys. Rev. B **83**, 193304 (2011).

[12] M. Zholudev, F. Teppe, M. Orlita, C. Consejo, J. Torres, N. Dyakonova, M. Czapkiewicz, J. Wróbel, G. Grabecki, N. Mikhailov, S. Dvoretskii, A. Ikonnikov, K. Spirin, V. Aleshkin, V. Gavrilenko, and W. Knap, Magnetospectroscopy of two-dimensional hgte-based topological insulators around the critical thickness, Phys. Rev. B **86**, 205420 (2012).

[13] L. Fu and C. L. Kane, Topological insulators with inversion symmetry, Phys. Rev. B **76**, 045302 (2007).

[14] C. Brüne, C. X. Liu, E. G. Novik, E. M. Hankiewicz, H. Buhmann, Y. L. Chen, X. L. Qi, Z. X. Shen, S. C. Zhang, and

L. W. Molenkamp, Quantum Hall Effect from the Topological Surface States of Strained Bulk HgTe, Phys. Rev. Lett. **106**, 126803 (2011).

[15] D. A. Kozlov, Z. D. Kvon, E. B. Olshanetsky, N. N. Mikhailov, S. A. Dvoretsky, and D. Weiss, Transport Properties of a 3D Topological Insulator Based on a Strained High-Mobility HgTe Film, Phys. Rev. Lett. **112**, 196801 (2014).

[16] C. R. Becker, V. Latussek, G. Landwehr, and L. W. Molenkamp, Inverted band structure of type-iii HgTe/Hg$_{1-x}$Cd$_x$Te superlattices and its temperature dependence, Phys. Rev. B **68**, 035202 (2003).

[17] N. N. Mikhailov, R. N. Smirnov, S. A. Dvoretsky, Y. G. Sidorov, V. A. Shvets, E. V. Spesivtsev, and S. V. Rykhlitski, Growth of hgcdte nanostructures by molecular beam epitaxy with ellipsometric control, Int. J. Nanotechnol. **3**, 120 (2006).

[18] S. Dvoretsky, N. Mikhailov, Y. Sidorov, V. Shvets, S. Danilov, B. Wittman, and S. Ganichev, Growth of HgTe quantum wells for IR to THz detectors, J. Electron. Mater. **39**, 918 (2010).

[19] A. M. Shuvaev, G. V. Astakhov, C. Brüne, H. Buhmann, L. W. Molenkamp, and A. Pimenov, Terahertz magneto-optical spectroscopy in HgTe thin films, Semicond. Sci. Technol. **27**, 124004 (2012).

[20] M. S. Zholudev, A. V. Ikonnikov, F. Teppe, M. Orlita, K. V. Maremyanin, K. E. Spirin, V. I. Gavrilenko, W. Knap, S. A. Dvoretskiy, and N. N. Mihailov, Cyclotron resonance in hgte/cdte-based heterostructures in high magnetic fields, Nanoscale Res. Lett. **7**, 534 (2012).

[21] C. Zoth, P. Olbrich, P. Vierling, K.-M. Dantscher, V. V. Bel'kov, M. A. Semina, M. M. Glazov, L. E. Golub, D. A. Kozlov, Z. D. Kvon, N. N. Mikhailov, S. A. Dvoretsky, and S. D. Ganichev, Quantum oscillations of photocurrents in hgte quantum wells with dirac and parabolic dispersions, Phys. Rev. B **90**, 205415 (2014).

[22] K.-M. Dantscher, D. A. Kozlov, P. Olbrich, C. Zoth, P. Faltermeier, M. Lindner, G. V. Budkin, S. A. Tarasenko, V. V. Bel'kov, Z. D. Kvon, N. N. Mikhailov, S. A. Dvoretsky, D. Weiss, B. Jenichen, and S. D. Ganichev, Cyclotron-resonance-assisted photocurrents in surface states of a three-dimensional topological insulator based on a strained high-mobility hgte film, Phys. Rev. B **92**, 165314 (2015).

[23] G. M. Gusev, E. B. Olshanetsky, Z. D. Kvon, A. D. Levin, N. N. Mikhailov, and S. A. Dvoretsky, Nonlocal Transport Near Charge Neutrality Point in a Two-Dimensional Electron-Hole System, Phys. Rev. Lett. **108**, 226804 (2012).

[24] G. M. Minkov, A. V. Germanenko, O. E. Rut, A. A. Sherstobitov, S. A. Dvoretski, and N. N. Mikhailov, Two-dimensional semimetal in a wide hgte quantum well: Magneto-transport and energy spectrum, Phys. Rev. B **88**, 155306 (2013).

[25] G. M. Minkov, A. V. Germanenko, O. E. Rut, A. A. Sherstobitov, S. A. Dvoretski, and N. N. Mikhailov, Hole transport and valence-band dispersion law in a hgte quantum well with a normal energy spectrum, Phys. Rev. B **89**, 165311 (2014).

[26] A. Jost, M. Bendias, J. Böttcher, E. Hankiewicz, C. Brüne, H. Buhmann, L. W. Molenkamp, J. C. Maan, U. Zeitler, N. Hussey, and S. Wiedmann, Electron–hole asymmetry of the topological surface states in strained hgte, Proc. Natl. Acad. Sci. USA **114**, 3381 (2017).

[27] G. M. Minkov, V. Y. Aleshkin, O. E. Rut, A. A. Sherstobitov, A. V. Germanenko, S. A. Dvoretski, and N. N. Mikhailov, Valence band energy spectrum of HgTe quantum wells with an inverted band structure, Phys. Rev. B **96**, 035310 (2017).

[28] G. M. Minkov, V. Y. Aleshkin, O. E. Rut, A. A. Sherstobitov, S. A. Dvoretski, N. N. Mikhailov, and A. V. Germanenko, Anisotropy of the in-plane *g*-factor of electrons in hgte quantum wells, Phys. Rev. B **101**, 085305 (2020).

[29] G. Minkov, V. Y. Aleshkin, O. Rut, A. Sherstobitov, A. Germanenko, S. Dvoretski, and N. Mikhailov, Spin-orbit splitting of the conduction band in hgte quantum wells: Role of different mechanisms, Physica E **110**, 95 (2019).

[30] M. König, S. Wiedmann, C. Brüne, A. Roth, H. Buhmann, L. W. Molenkamp, X.-L. Qi, and S.-C. Zhang, Quantum spin hall insulator state in hgte quantum wells, Science **318**, 766 (2007).

[31] A. Roth, C. Brüne, H. Buhmann, L. W. Molenkamp, J. Maciejko, X.-L. Qi, and S.-C. Zhang, Nonlocal transport in the quantum spin hall state, Science **325**, 294 (2009).

[32] G. M. Gusev, Z. D. Kvon, O. A. Shegai, N. N. Mikhailov, S. A. Dvoretsky, and J. C. Portal, Transport in disordered two-dimensional topological insulators, Phys. Rev. B **84**, 121302(R) (2011).

[33] G. M. Minkov, A. A. Sherstobitova, A. V. Germanenko, O. E. Rut, S. A. Dvoretskii, and N. N. Mikhailov, Conductance of a lateral p-n junction in two dimensional hgte structures with an inverted spectrum the role of edge states, Pisma Zh. Eksp. Teor. Fiz. **101**, 522 (2015) [JETP Lett. **101**, 469 (2015)].

[34] J. E. Moore and L. Balents, Topological invariants of time-reversal-invariant band structures, Phys. Rev. B **75**, 121306(R) (2007).

[35] M. Z. Hasan and C. L. Kane, *Colloquium*: Topological insulators, Rev. Mod. Phys. **82**, 3045 (2010).

[36] X.-L. Qi and S.-C. Zhang, Topological insulators and superconductors, Rev. Mod. Phys. **83**, 1057 (2011).

[37] E. B. Olshanetsky, Z. D. Kvon, G. M. Gusev, A. D. Levin, O. E. Raichev, N. N. Mikhailov, and S. A. Dvoretsky, Persistence of a Two-Dimensional Topological Insulator State in Wide HgTe Quantum Wells, Phys. Rev. Lett. **114**, 126802 (2015).

[38] H. Zhang and S.-C. Zhang, Topological insulators from the perspective of first-principles calculations, Phys. Status Solidi RRL **7**, 72 (2013).

[39] C. Brüne, C. Thienel, M. Stuiber, J. Böttcher, H. Buhmann, E. G. Novik, C.-X. Liu, E. M. Hankiewicz, and L. W. Molenkamp, Dirac-Screening Stabilized Surface-State Transport in a Topological Insulator, Phys. Rev. X **4**, 041045 (2014).

[40] D. A. Kozlov, Z. D. Kvon, M. L. Savchenko, D. Weiss, N. N. Mikhailov, and S. A. Dvoretskii, Three-dimensional topological insulator based on a strained hgte film, Low Temp. Phys. **41**, 82 (2015).

[41] M. L. Savchenko, D. Kozlov, Z. Kvon, N. N. Mikhailov, and S. A. Dvoretskii, Pis'ma Zh. Eksp. Teor. Fiz. **104**, 311 (2016) [JETP Lett. **104**, 302 (2016)].

[42] D. A. Kozlov, D. Bauer, J. Ziegler, R. Fischer, M. L. Savchenko, Z. D. Kvon, N. N. Mikhailov, S. A. Dvoretsky, and D. Weiss, Probing Quantum Capacitance in a 3D Topological Insulator, Phys. Rev. Lett. **116**, 166802 (2016).

[43] J. Ziegler, D. A. Kozlov, N. N. Mikhailov, S. Dvoretsky, and D. Weiss, Quantum Hall effect and Landau levels in the three-dimensional topological insulator HgTe, Phys. Rev. Research **2**, 033003 (2020).

[44] N. C. Mamani, G. M. Gusev, O. E. Raichev, T. E. Lamas, and A. K. Bakarov, Nonlinear transport and oscillating

magnetoresistance in double quantum wells, Phys. Rev. B **80**, 075308 (2009).

[45] O. E. Raichev, Magnetoresistance oscillations in two-subband electron systems: Influence of electron-phonon interaction, Phys. Rev. B **81**, 195301 (2010).

[46] I. M. Lifshits and A. M. Kosevich, Theory of magnetic suscep-tibility in metals at low temperatures, Zh. Eksp. Teor. Fiz. **29**, 730 (1955) [Sov. Phys.–JETP **2**, 636 (1956)].

[47] G. M. Minkov, O. E. Rut, A. A. Sherstobitov, S. A. Dvoretski, N. N. Mikhailov, V. A. Solov'ev, M. Y. Chernov, S. V. Ivanov, and A. V. Germanenko, Magneto-intersubband oscillations in two-dimensional systems with an energy spectrum split due to spin-orbit interaction, Phys. Rev. B **101**, 245303 (2020).

[48] J. Los, A. Fasolino, and A. Catellani, Generalization of the k·p approach for strained layered semiconductor structures grown on high-index-planes, Phys. Rev. B **53**, 4630 (1996).

[49] C. R. Becker, V. Latussek, A. Pfeuffer-Jeschke, G. Landwehr, and L. W. Molenkamp, Band structure and its temperature de-pendence for type-iii HgTe/Hg$_{1-x}$Cd$_x$Te superlattices and their semimetal constituent, Phys. Rev. B **62**, 10353 (2000).

[50] K. Takita, K. Onabe, and S. Tanaka, Anomalous magnetoresis-tance and band crossing in uniaxially compressed HgTe, Phys. Status Solidi B **92**, 297 (1979).

[51] E. Ivchenko, *Optical Spectroscopy of Semiconductor Nanos-tructures* (Alpha Science International, Harrow, UK, 2005), p. 427.

[52] See Supplemental Material at http://link.aps.org/supplemental/10.1103/PhysRevB.106.085301 for theoretical details.

[53] V. Y. Aleshkin, A. Germanenko, G. Minkov, and A. Sherstobitov, Anomalous electron polarizability of HgTe quan-tum wells, Physica E (Amsterdam) **128**, 114606 (2021).

[54] T. Andlauer and P. Vogl, Full-band envelope-function approach for type-ii broken-gap superlattices, Phys. Rev. B **80**, 035304 (2009).

[55] J. Zhu, C. Lei, and A. H. MacDonald, Electronic properties of thin films of tensile strained HgTe, arXiv:1804.01662.